Wire Based Directed Energy Deposition of JBK-75

J.A. SCHNEIDER, G. PUERTO, E. WALKER, B.T. MONTGOMERY, P.R. GRADL, B. WALKER, M. SANTANGELO, and S. THOMPSON

Applications and adoption of metal additive manufacturing (AM) are increasing for fabrication of low volume, complex components with novel materials, as well as replacement parts. While the use of powder bed fusion-based processes have been widely used to build complex components with fine feature resolution, there is a volume limitation. Expanding the application of metal AM will rely on other processes that remove this build size constraint. These processes are referred to as Directed Energy Deposition (DED) and can use either powder or wire feedstock. Wire based DED provides the highest deposition rates which shortens the fabrication time making it attractive for fabrication of large parts replacing traditional wrought billets or castings. In this study, an iron-based austenitic superalloy (JBK-75) was deposited using an arc-based, wire-fed (AW)-DED process. The material was metallographically characterized and quasi-static mechanical properties were obtained. The resulting microstructure and mechanical properties are compared with conventional wrought and cast forms of JBK-75 subjected to the same heat treatments. As compared to wrought material, the AW-DED grain size was larger after the heat treatment, although the strengths were similar. Improved homogenization was observed after heat treatment in the AW-DED specimens as compared to the cast specimens.

I. INTRODUCTION

THE second industrial revolution prompted the improvement of steel (Fe) alloys to obtain higher strength and resistance to corrosion to meet the needs of steam powered equipment as they could be operated up to 700 °C without significant loss of strength.[1,2] Resistance to corrosion was obtained by a critical ratio of nickel (Ni) and chromium (Cr) additions to the Fe to stabilize the austenitic matrix resulting in the 3xx series of stainless steels.[1,3] The retention of the austenitic (γ) phase of Fe eliminated potential phase transformations over a range of temperatures from cryogenic to its melting point. Thus, the family of 3xx series, austenitic stainless steels found wide application due to its corrosion resistance, strength, and their ability to be cast, forged, machined, and fusion welded. Since austenitic steels are also resistant to hydrogen environment embrittlement (HEE), methods to develop Fe based superalloys for high pressure hydrogen environments were pursued.[4,5]

Additional strengthening in the initial family of 3xx series austenitic stainless steels relied on either strain hardening and/or Hall Petch grain size strengthening. Further increases to the strength of this alloy explored the addition of Ti for precipitation strengthening of the γ' $Ni_3(Ti, Al)$ phase during subsequent aging heat treatments.[2,3,6–8] The initial precipitation strengthened austenitic steel was developed by Allegheny Ludlum Steel Corporation in 1951 and designated A-286.[8,9] Sufficient hardening was obtained with a Ti content between 1.3 and 2.4 pct, when aged in the range between 593 °C and 871 °C.[7,10,11] The primary phases present in A-286 were TiC, γ' and η.[2,3,8,12]

While A-286 drastically improved the strength of austenitic steels, early studies found the alloy to be highly susceptible to heat-affected zone (HAZ) microfissuring as well as hot cracking within the fusion zone.[13–16] The hot cracking was attributed to the formation of a low melting eutectic comprised of the matrix Fe and a $Fe_2(Ti,Mo)$-type Laves phase along grain boundaries.[13–15] The cracking issues were further exasperated if continuous layers of TiC segregated along grain boundaries since the Laves phase nucleated largely around decomposing TiC.[12,16] As multi-piece, complex assemblies rely on fusion welding to join various components, the use of A-286 was limited.

J.A. SCHNEIDER, G. PUERTO, E. WALKER, and B.T. MONTGOMERY are with the Department of Mechanical Engineering, University of Alabama in Huntsville, Huntsville, AL 35899. Contact e-mail: jas0094@uah.edu P.R. GRADL is with the NASA Marshall Space Flight Center, Huntsville AL, 35812. B. WALKER and M. SANTANGELO are with the Keystone Synergistic Enterprises, Port Saint Lucie FL, 34953. S. THOMPSON is with the Materials Science and Engineering Division, Propulsion and Structures Technology, Development Directorate FCDD-AMT-MPS, Huntsville AL, 35808.

Various studies in both fusion welding and casting noted that the Laves and a detrimental Ni_3Ti (η) phase formed in segregated regions during solidification.[13–16] Thus, slight chemistry modifications were pursued by properly selected weld wire to improve the properties and quality of the melt pool.[10,16] To alleviate the microfissuring issues that occurred during fusion welding of A-286, elemental modifications were made, which resulted in JBK-75.[10,16,17] The susceptibility of Laves phase formation was minimized by reducing the phosphorus (P), sulfur (S), boron (B) and silicon (Si) content. The Carbon (C) content was reduced to minimize the formation of a continuous, detrimental layer of TiC along grain boundaries while still promoting the formation of TiC strengthening particles. As austenitic steels are also used for hydrogen storage, the elemental modifications of Al, Ti and Mo for improving weldability and strength was balanced against their effects on HEE compatibility.[4,18] Once the JBK-75 chemistry was established for promoting the γ' strengtheners while minimizing TiC and η content, various heat treatments investigated were reported in the literature. As the cellular η phase was noted to decrease hydrogen compatibility, the aging temperature was kept below 800 °C to reduce its formation.[18]

Subsequent studies confirmed that although the performance of JBK-75 could be controlled through the microstructure, it was also highly dependent on the thermomechanical processing paths and heat treatments.[19–22] Ultimately, control of the resulting phases was found to be a function of the initial solidification structure and microsegregation.[23–27] During solidification, Ti, C, Si and Mo tend to segregate in interdendritic regions. These regions, if unhomogenized either through heat treatment and thermomechanical working, became suitable sites for the nucleation of cellular η as well as Laves phases.[23] Various studies found that holding the optimal Ti content to below 3 pct provided effective strengthening, while keeping the ratio of Ni/(Ti + Al) below 10 to minimize the tendency for η phase nucleation.[6,7,18,23] In addition to control of the chemistry, various thermomechanical processes were also effective for eliminating any retained η phase.

The resulting JBK-75 alloy could be cast, fusion welded, and forged to form various components.[10,16,19,21] Further utilization of the family of austenitic, precipitation strengthened stainless steels relies on evaluating its applicability toward other manufacturing processes including the use of various AM processes. While this study focuses on AW-DED, traditional wrought and cast forms were included for comparison which comprise the three forms of JBK-75 evaluated.

Alloy compositions presented in Table I highlight the alloying changes from the wrought, single phase austenitic stainless steel 316L to the precipitation strengthened A-286 and JBK-75. Since various studies have shown that slight chemistry modifications and thermomechanical processing significantly reduces cracking susceptibility,[10,16] the chemistries of the precipitation strengthened A-286 and JBK-75 continue to be modified in accordance with the processing routes.

Many current studies simply refer to these alloys as commercial A-286 vs modified A-286.[19–21,23,25–27]

Table II compares heat treatment schedules developed for wrought A-286 vs wrought and cast JBK-75.[28,29] As JBK-75 was a derivative of A-286, the heat treatment schedules are similar. In the forging process, homogenization is achieved through thermomechanical working which also refined the grain size.[19,20] Castings used a separate homogenization heat treatment that could also be accomplished through a hot isostatic pressing (HIP) for minimizing porosity. The full heat treatment (FHT) condition for the precipitation strengthened alloys includes solutionizing and aging. The formation of the η phase is noted to be pronounced at extended times above 800 °C[18,24,30] with minimal η formation at temperatures below 740 °C.[24] Thus the aging heat treatment is done at 720 °C

II. MATERIALS AND METHODS

Figure 1 illustrates the AW-DED process used in this study which is based on a Metal Inert Gas (MIG) fusion welding process. This process has alternately been referred to in the literature as wire arc additive manufacturing (WAAM).[31,32] In this process, the wire forms an eroding electrode to form the arc, surround by localized argon purge gas to reduce the potential for oxidation in the melt pool. The wire feedstock used can be a solid wire or a cored wire in the diameter range of 0.08 to 0.16 cm (0.032″ to 0.062″), respectively.[33–35] The cored wire uses a metal sheathing in which a mix of elemental powders are blended and packed to obtain the desired chemistry. Use of a cored wire provides a low-cost approach for alloy modifications in AM processing in addition to avoiding contamination resulting from weld wire flux coatings. The cored wire used in this study was fluxless with a diameter of 0.16 cm.

Figure 2 shows the cylindrical specimens fabricated for this study using the AW-DED process with fluxless cored wire procured from Polymet.[35] The AW-DED AM system was mounted on a robotic platform using a FANUC robot integrated to a Lincoln Electric pulsed-arc MIG system. Fluxless cored wire was fed at a rate of 430 to 470 cm/min at a deposition rate of 4.3 kg/h (9.5 lb/h) with a stick out length of 3 mm (0.13″). The deposition height for each layer was monitored using a Keyence Laser Displacement Sensor (LK-G5000). A pulse transfer mode was used in which a DC waveform is produced with a distinct ramp profile to achieve spray transfer, followed by a decay down to normal globular transfer power levels for detachment of the molten weld droplet. This results in a fluctuating voltage with a root-mean-square (RMS) value of 22 V and nominal 330 amps. A single pass, weave pattern was used to deposit the cylinders with a 15.24 cm (6″) diameter, 17.78 cm (7″) height and a 1.27 cm (0.5″) wall thickness. The cylinders were deposited on rectangular stainless steel 316 plates that were 19 mm (0.75″) thick and wide enough to accommodate clamping. An interpass temperature of 260 °C was used to maintain the heat profile during the build and minimize distortion and cracking.

Table I.   Comparison of Nominal Elemental Composition for the Wrought Austenitic Stainless Steel Family

	Fe	Ni	Cr	Ti	Al	Mn	Mo	V	C	B
SS 316L UNS S31603	68.5	12	17	—	—	2.5			≤ 0.03	
A-286 UNS 66286[28]	54.32	24.0–27.0	13.5–16.0	1.9–2.35	0.35	2.0	1.0–1.5	0.1–0.5	0.08	0.003–0.010
JBK-75[17]	52.08	29.0	14.75	2.10	0.23	0.25	1.25	0.30	0.03	0.0015

Table II.   Heat Treatment Schedule Comparison for Precipitation Strengthened, Austenitic Stainless Steels

Heat Treatment Step	Wrought A-286 Temperature (°C)/Time (h)[28]	JBK-75 Wrought Temperature (°C)/Time (h)[4]	JBK-75 Cast Temperature (°C)/Time (h)[29]
Homogenization (and/or HIP)	—	—	1120 ±25/4
Solution	982 + 14/2 h oil quench	980 ± 25 / 1 rapid air quench	980 ± 25/4 rapid air quench
Aging	718 + 8/≤ 16 air cool	720 ± 25 / 16 air cool	720 ±25/16 air cool

Fig. 1—AW-DED Schematic.

Fig. 2—JBK-75 Cored Wire Build.
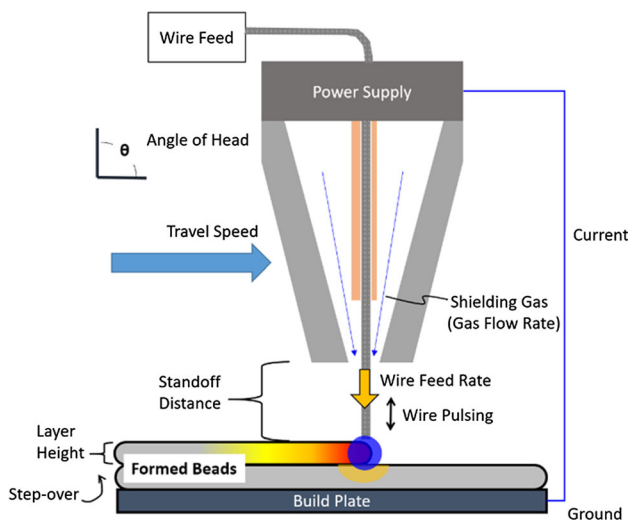
The interpass temperature was controlled by pausing the process until the measured temperature had fallen under the target limit of 260 °C. No external cooling was applied during the build. Temperature measurements were made with a Micro-Epsilon thermometer CT Laser M1, infrared pyrometer, mounted to the robotic welding torch to maintain a fixed focal length.

The starting elemental chemistry of the feedstock and final deposition was obtained using Inductively Coupled Plasma (ICP) optical emission spectroscopy (OES) per ASTM E3047.[36] The lighter elements were analyzed using combustion per ASTM E1019[37] for carbon and inert gas fusion (IGF) for oxygen and nitrogen. The same analysis was completed for all three forms of the JBK-75 alloy including the wrought and cast forms.
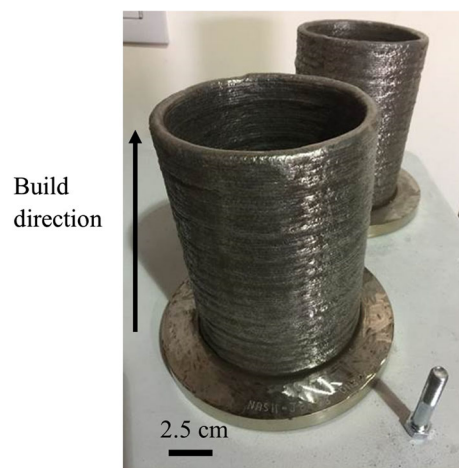
After deposition, a 10 cm (4 inch) tall section nearest the build plate was removed and machined into test specimens with the geometry as shown in Figure 3(a). After machining, the test specimens were heat treated in vacuum. Although AM parts are often subjected to an initial stress relief heat treatment to relieve resulting residual stresses, especially for thin walled structures, it was not incorporated into this study on AW-DED specimens. As the AW-DED process targets larger components that often exceed the capacity of most HIP furnaces, only a homogenization heat treatment was conducted at 1190 °C. After holding for 4 h, the furnace was cooled to 980 °C and held for 1.5-hours for solutionizing. The specimens were then argon quenched to a temperature below 149 °C and then aged at 720 °C for 16 hours followed by air cooling. To duplicate time
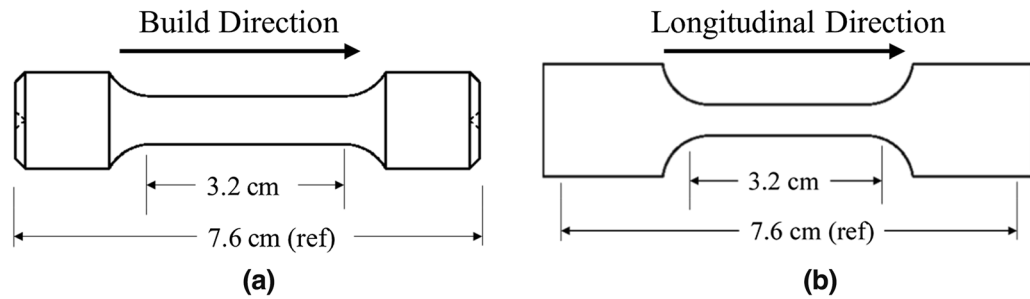
Fig. 3—Nominal geometries for the tensile specimens showing (*a*) round and (*b*) flat.

and temperatures, all three forms of JBK-75 were subjected to the same heat treatment.

Tensile specimens were machined from the AW-DED build with the tensile axis aligned with the build direction. The nominal dimensions are shown in Figure 3(a) with a nominal gage diameter of 0.6 cm along a 3.2 cm gage length. The grip portions have a 13 cm (0.5″) diameter. Tension tests were conducted on 25 samples of the AW-DED at temperatures ranging from − 195.5 to 649 °C with five (5) round specimens tested at each temperature. All tension tests were conducted at a constant crosshead velocity of 0.13 cm/min per ASTM E8/E8M.[38] Rockwell B hardness data was also obtained using a Rockwell Model 574 tester in accordance with ASTM Standard E18.[39] A total of 12 hardness measurements were made for each of the JBK-75 forms including the AW-DED, wrought, and cast.

For comparison with the AW-DED, additional flat tensile samples were machined from cast and wrought JBK-75 with the tensile axis aligned with the longitudinal direction. Nominal dimensions for the flat samples are shown in Figure 3(b) with a nominal gage cross section of 0.6 × 0.6 cm. The wrought and cast samples were subjected to the same FHT schedule as was used for the AW-DED. A total of 5 samples were tested at 25 °C for the cast and wrought samples using the same procedure as for the AW-DED.

Excess material from machining of the test specimens from all three forms were mounted in a phenolic and prepared for metallographic characterization. Two orientations of each sample, longitudinal and transverse, were prepared to evaluate potential anisotropic nature of the microstructure. The preparation followed metallurgical standard practices with a final polish of 1 μm diamond solution. Once the specimens were polished, a Zeiss AXIO Vert. A1 Inverted Microscope was used to obtain images. Sufficient images were obtained using a 5X objective for a void analysis based on the feret diameter for approximately 100 voids.[40] The area fraction was obtained from the void area normalized by the area of the images. All analysis used Fiji ImageJ version 2.13.1 software for determining the area fraction, feret diameter, circularity, and aspect ratio of the voids.

To remove potential oxide layer formation and to reveal grain boundaries, the specimens were repolished using a 1 μm diamond solution for 10 seconds before etching using Waterless Kallings. Grain sizes were based on the feret diameter. Sufficient images were obtained for the analysis using approximately 100 grains.

After recording optical microscopy images, only the AW-DED build plane (XY) specimens were prepared for scanning electron microscope (FE-SEM) and elemental analysis using energy-dispersive X-ray spectroscopy (EDS). The sample was electropolished to remove the etchant. A Struers LectroPol-5 electropolisher was set at 35 V at a setting of 13 for the flow rate for 10 to 15 seconds. The electrolyte used was a mixture of 58.8 pct Methanol (382 mL), 35.5 pct Ethylene glycol monobutyl ether (229 mL), & 5.9 pct Perchloric acid (39 mL) electrolyte maintained at 22 °C. Back scattered electron (BSE) Images were obtained on a Hitachi SU5000 field emission, FE-SEM with Oxford EDS for elemental mapping.

For investigation of minor phases present, X-ray diffraction was conducted on all three forms using a Seifert 3000 PTS X-ray diffractometer (XRD) with a 50 scan/channel semiconductor detector. The XRD was configured with a Co Kα source and was operated at 40 kV and 40 mA over the 2-theta range of 25 to 120 deg with a step scan of 0.013 deg for 1200 s. Slow scans were used to investigate the presence of minor phases. AW-DED JBK-75 build plane samples (XY) were analyzed in the as-built condition and after the FHT. For comparison, a similar XRD analysis was obtained for the transverse plane of the wrought and cast specimens after the FHT.

III. RESULTS

Table III summarizes the elemental composition of the 3 forms of the JBK-75 used in this study as compared to the original patent. Although oxygen and nitrogen levels were not defined in the original patent, they were included since oxidation is a concern in AM processing.

Results from the void analysis of the AW-DED samples are summarized in Table IV. After the FHT, a slight increase in the feret diameter can be observed along with an increase in area percentage. The corresponding increase in aspect ratio and decrease in circularity indicates an elongation of the initial voids. This increase is attributed to expansion of trapped gas during the subsequent heat treatments.

Table III. Composition of JBK-75 Forms Used in this Study as Compared to Original Patent

Sample ID	JBK-75 [17]	AW-DED AM	Cast	Wrought
Iron	44.78–59.39	Balance (54.3)	50.89	51.67
Nickel	24–34	29.23	29.85	29.52
Chromium	13.5–16.0	12.53	14.90	14.26
Silicon	0.01	0.21	0.018	0.110
Carbon	0.01–0.05	0.02	0.006	0.019
Aluminum	0.15–0.35	0.16	0.199	0.263
Titanium	1.9–2.3	1.42	2.37	2.27
Molybdenum	1.0–1.5	1.63	1.23	1.23
Vanadium	0.1–0.5	0.36	0.266	0.315
Nitrogen	—	0.044	0.002	0.003
Oxygen	–	0.04	0.002	0.001
Boron	0.0015	< 0.01	0.002	0.002
Manganese	0.25	—	0.048	0.074
Sulfur	0.03	0.005	0.005	0.001
Phosphorus	0.04	0.05	< 0.005	< 0.005

Table IV. Void Analysis for the AW-DED Specimens in the As-Built and FHT Conditions

AW-DED Samples	Percent Area	Circularity	Feret Diameter (μm)	Aspect Ratio
As-Built XY	0.12 ± 0.05	0.95 ± 0.02	5.04 ± 0.83	1.35 ± 0.06
As-Built Z	0.09 ± 0.01	0.95 ± 0.02	4.70 ± 0.06	1.45 ± 0.18
FHT XY	0.22 ± 0.07	0.8 ± 0.06	8.64 ± 2.06	1.69 ± 0.06
FHT Z	0.17 ± 0.02	0.81 ± 0.03	8.81 ± 0.47	1.66 ± 0.06
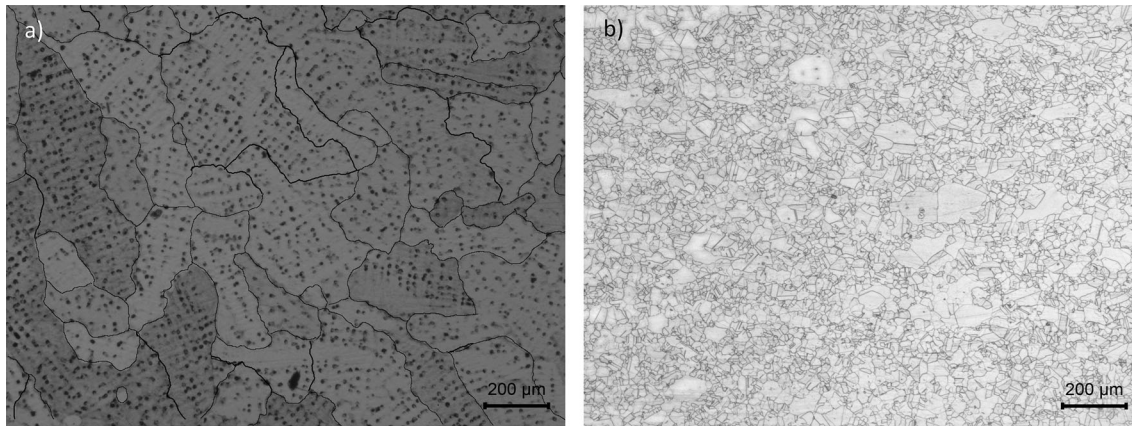
Fig. 4—Optical images of the transverse sections of the (*a*) cast vs (*b*) wrought specimens in the FHT condition. Note grain boundaries have been enhanced for the cast microstructure.

Optical images in Figures 4(a) and (b) compare the microstructure of the transverse section of FHT specimens for cast and wrought JBK-75, respectively. The wrought material shows a very fine grain size structure in comparison to the cast material. A finer grain size is attributed to thermomechanical processing used to produce plate form. Figures 5(a) and (b) shows the AW-DED XY build plane metallography for the as-built vs FHT condition showing some grain refinement after the FHT. From the grain size analysis, the resulting average diameter was 222 ± 39 μm for the AW-DED as compared to 378 + 261 μm for the cast corresponding to an ASTM grain size range of G = 1.25 to 0.0, respectively.[40] The wrought material had a finer grain size of 15.2 ± 2.2 with a corresponding G = 9.0.

SEM BSE are shown in Figure 6 for the as-built microstructure compared to after the FHT. These show the representative regions used for the elemental mapping. In general little difference was noted as the grain boundaries were clean with no evidence of elemental segregation or other phase formations. Various dark
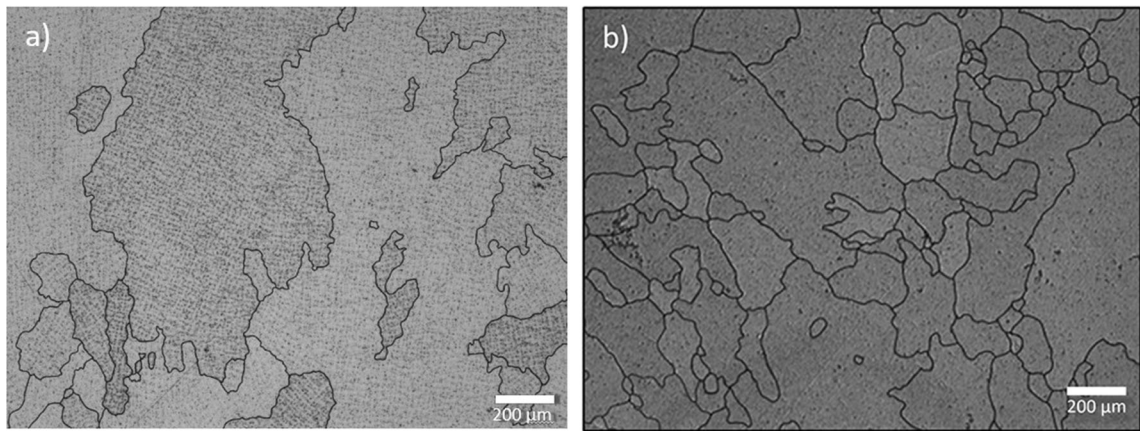
Fig. 5—Optical images of the AW-DED JBK-75 XY build plane microstructure for (*a*) as-built and (*b*) after FHT. Note grain boundaries have been enhanced.
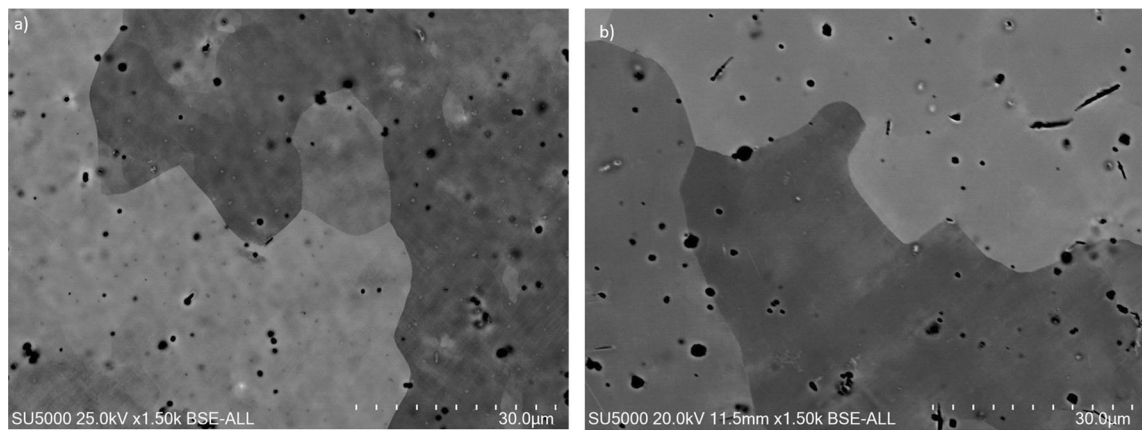

Fig. 6—Higher magnification SEM BSE to isolate region of interest for the elemental mapping. (*a*) as-built and (*b*) the FHT microstructures.

regions are observed that are either secondary phases or voids. Some acicular dark regions are also observed, especially in the as-built specimen.

Elemental maps are shown in Figure 7 for the as-built image in Figure 6a and in Figure 8 for the FHT specimen in Figure 6(b). The acicular phases are shown to be enriched in Mo. Some of the round phases are shown to be enriched in Ti, helping to distinguish between secondary phases and voids.

By comparison with Figure 7, Figure 8 shows similar distribution of Ti in the round secondary phases with some Mo and Al enrichment. These dark particles are interpreted to be either TiC or TiN dispersed within the grains. After the FHT, the Fe mapping shows possible depletion along what are interpreted as sub-boundaries.

As no evidence of Ti enrichment was observed in the elemental maps along the grain boundaries, data was collected along 15 μm long line scans within grains and across grain boundaries as summarized in Table V. The line scans were conducted in the as-built and FHT specimens. Some minor elemental variation is noted in within the grains, but it is not considered to be an appreciable difference. Similar results are also noted in for the line scans across the grain boundary, confirming the absence of Ti segregation.

Although the grain boundary regions were noted in general to be free of any secondary phases, one isolated region of a lamellar formation was observed along a grain boundary as shown in Figure 9 in the AW-DED as-built condition. Extending from this lamellar formation, dark deposits can be observed along an adjacent grain boundary. Figure 10 shows a magnified image of this region. Although the features observed were too fine to obtain an elemental map, the dark regions in the BSE SEM image could correspond to either Ti or Mo as was evidenced in dark secondary particles in Figures 7 and 8. This lamellar structure is similar in appearance to the cellular structure of the η phase.[4,24,25,27,41]

Table VI lists the possible phases of interest in this study and the corresponding International Center for Diffraction Data (ICDD) powder diffraction files (PDF) files used for indexing. A comparison of the XRD scan for the AW-DED is shown in Figure 11 for the as-built vs FHT AW-DED specimens showing the {100} texture of the as-built specimen is retained. There are no resolvable peaks associated with minor phases in the as-built specimen with the possible exception of TiO_2.
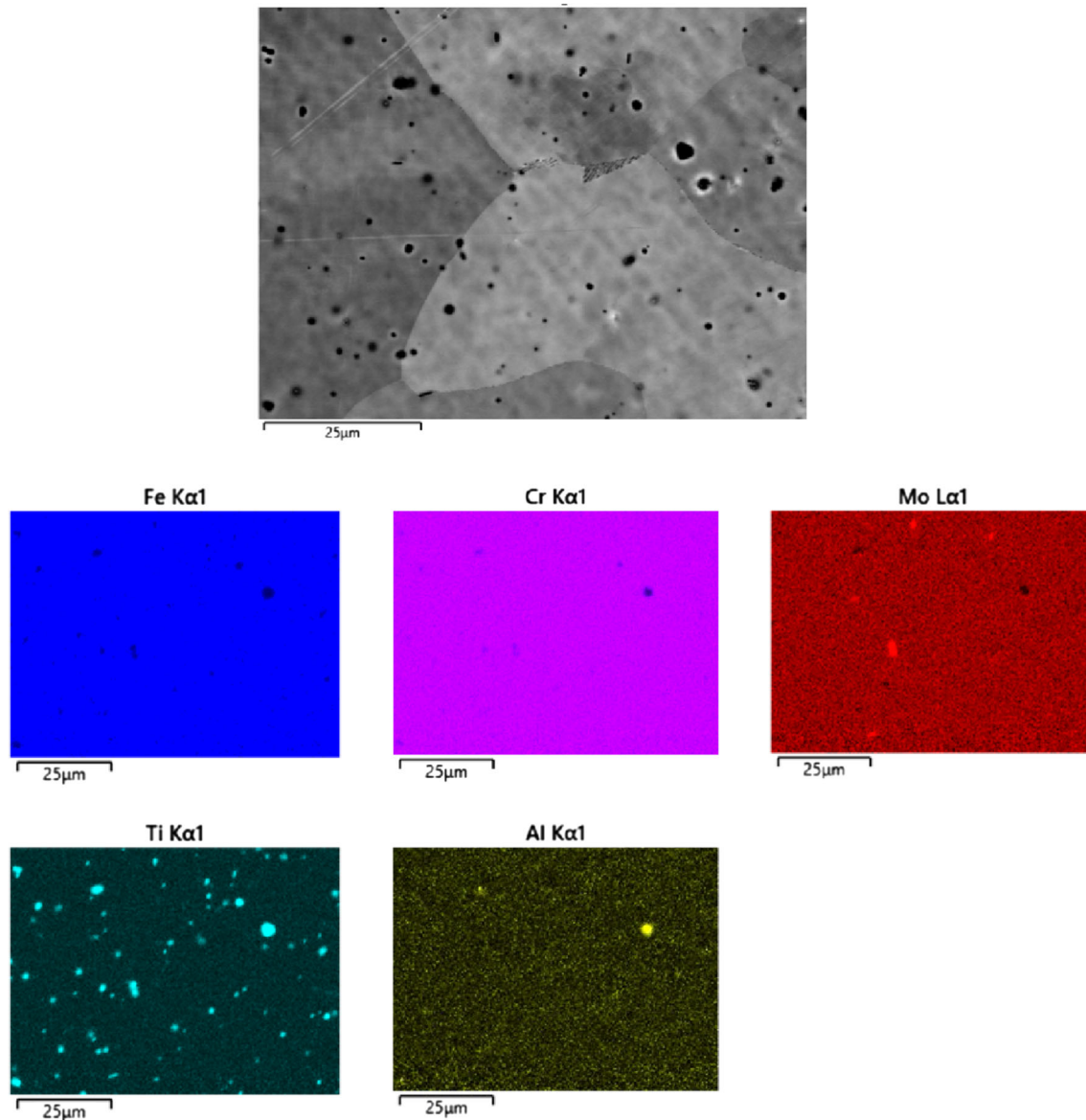
Fig. 7—Elemental mapping of the as-built AW-DED specimen.

After the FHT, there is a very slight increase in the TiO_2 content in addition to the appearance of Ti(C,N). Although a protective environment is used to shield the metal deposition, some oxidation can occur coinciding with the detection of TiO_2 in the as-built which may coarsen during subsequent heat treatments, becoming more observable.

After the FHT, a comparison of the three forms of the JBK-75 are shown in Figure 12. Comparing the peak intensities to the ICDD PDF powder files, the wrought material is consistent with a randomly oriented microstructure. Strong textures are noted in both the AW-DED and the cast, although they are of different natures. The AW-DED has a {100} texture, typical of other face centered cubic, metal AM structures.[42] In contrast, the cast specimen shows a predominant {311} texture.

To better resolve the minor peaks, an expanded view for the 3 forms of JBK-75 is presented in Figure 13. Due to minor amounts, it is difficult to distinguish between TiC or TiN since several of their peaks overlap, thus both phases could be present. No evidence of η formation is observed in the XRD analysis of any of the forms of JBK-75 processed indicating negligible presence.

Table VII summarizes the Rockwell B hardness values with the empirically correlated strength.[43] Since AM processes contain voids, their effect on resulting tensile properties can be qualitatively accessed by comparison of the values. The hardness data indicates the highest strength is expected in the AW-DED with the wrought having the lowest.

Figure 14 compares the tensile properties of the three forms of the JBK-75 at room temperature. Similar to the hardness readings in Table VII, the AW-DED specimen
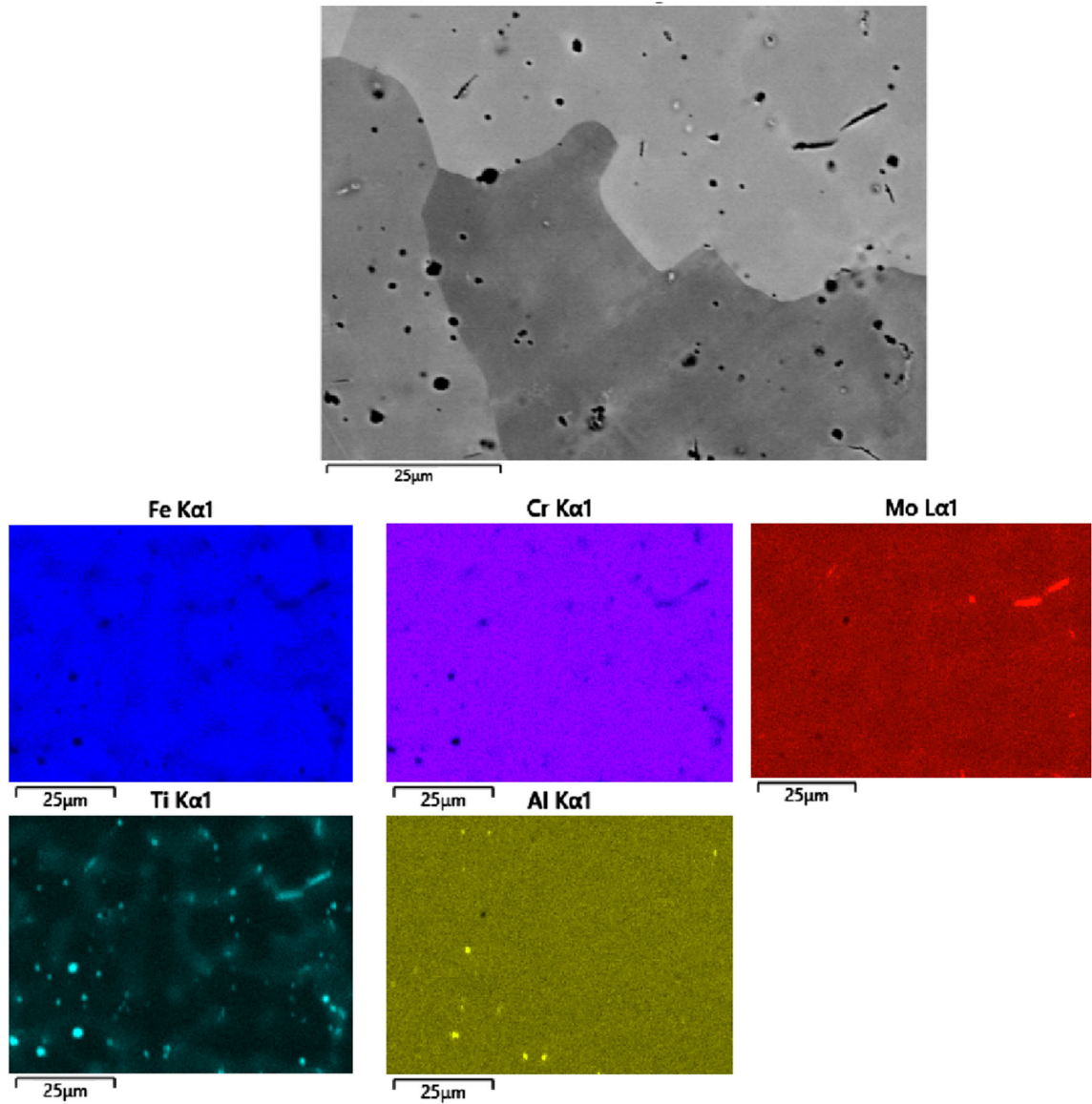
Fig. 8—Elemental mapping of the FHT AW-DED specimen.

Table V. Summary of Line Scan Data Across Grains and Grain Boundaries, Given as Weight Percent

	Grains		Grain Boundaries	
	As-Built	FHT	As-Built	FHT
Fe	44.68 ± 1.14	45.43 ± 2.10	44.59 ± 0.75	46.60 ± 1.40
Ni	28.14 ± 0.99	28.29 ± 1.27	28.19 ± 0.65	27.92 ± 0.90
Cr	14.68 ± 0.57	14.90 ± 0.38	14.63 ± 0.37	15.20 ± 0.38
Ti	1.50 ± 0.22	1.95 ± 0.70	1.55 ± 0.15	1.50 ± 0.45
Al	0.20 ± 0.18	0.20 ± 0.10	0.20 ± 0.14	0.18 ± 0.11
Mo	1.27 ± 0.46	1.45 ± 0.30	1.24 ± 0.28	1.39 ± 0.31
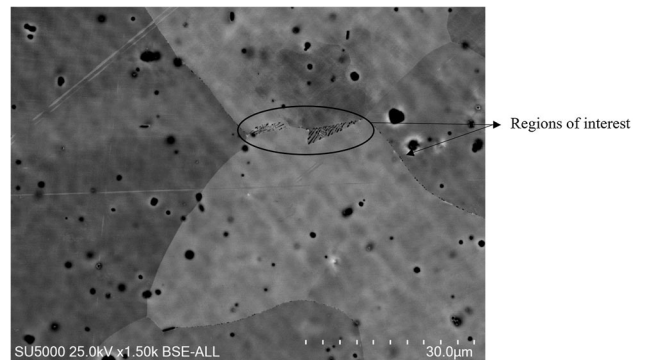
Fig. 9—Region showing cellular structure along the grain boundary in the as-built specimen.

shows higher tensile and yield strength as compared to the cast and wrought forms. The cast form has the highest elongation to failure with the wrought having the lowest value. Since the hardness values correspond empirically to the measured strength, this is taken as an indication that the small amount of AW-DED internal voids did not affect the tensile properties.
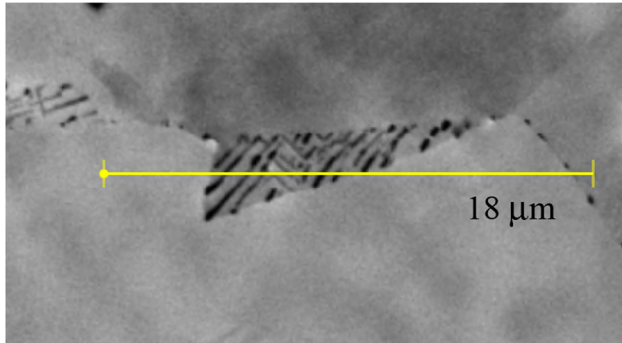

Fig. 10—Close up of cellular structure circled in Fig. 9.

The effect of test temperature was only evaluated for the AW-DED specimens which is summarized in Figure 15. As expected, the strength is noted to be highest at cryogenic temperatures (– 196 °C). As the temperature is increased above 25 °C, a slight decrease in strength is noted up to the maximum operating temperature of 650 °C.

IV. DISCUSSION

The materials used in this study compared three forms of JBK-75: wrought, cast, and AW-DED. As temperature and time can affect the final microstructure, all three forms were subject to the same heat treatment that included the homogenization step at 1190 °C.[4,29] Following homogenization, the specimens were solutionized at 980 °C, quenched and aged at 720 °C for 16 hrs. Figure 14 shows the resulting strengths after the FHT of homogenization, solutionization and aging, were similar in all three forms with slightly higher strength in the AW-DED and slightly higher ductility in the cast. While

Table VI. Potential Secondary Phases in Precipitation Stainless Steels

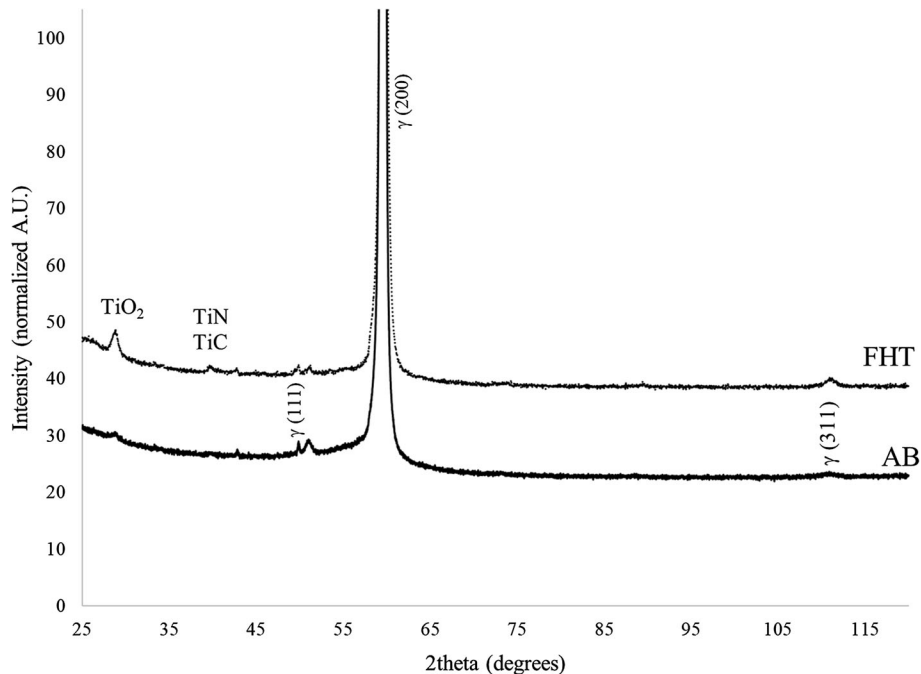| Phase	Composition	Crystal Structure	ICDD PDF #
γ	Ni-Fe-Cr	A1	00-052-0513
γ'	$Ni_3 (Ti,Al)$	$L1_2$	04-004-7762
η	$Ni_3 Ti$	$D0_{24}$	00-005-0723
Laves	$Fe_2 Mo$	C14	04-004-7304
Nitrides	$(\overline{Ti,Cr}) N$	HP8, CF8	00-038-1420
Carbides	$(\overline{Ti,Mo}) C$	A1	00-031-1400
Oxides	TiO	brookite (orthorhombic)	00-015-0875
	Al_2O_3	corundum (rhombohedral)	00-005-0712

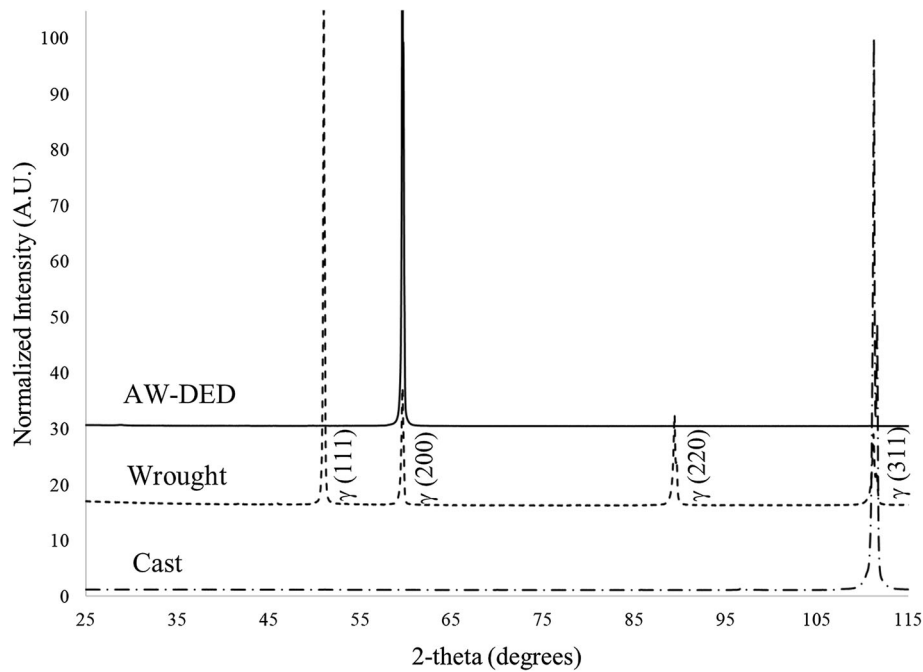Fig. 11—Phases in the as-built and FHT AW-DED JBK-75 specimens.

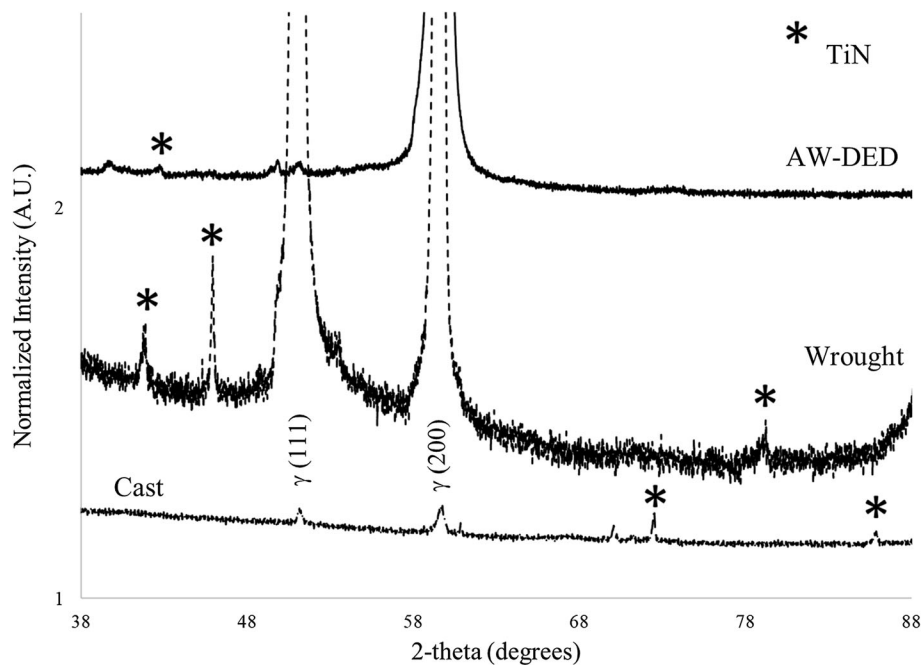Fig. 12—Comparison of the three forms of JBK-75 after the FHT.

Fig. 13—Expanded region to identify minor peaks in different forms of JBK75 specimens after the FHT.

the mechanical properties were similar, there was a vast change in the resulting microstructures of the three forms.

The finest grain size of 15 μm was found in the wrought material as a result of its prior thermomechanical working that also effectively homogenized the material.[11] Larger grain sizes were observed in the AW-DED and cast samples. After the FHT, the grain diameter for the AW-DED was approximately 222 μm as compared to the cast grain diameter of 378 μm diameter.

Although the grain size and morphology was similar between the cast and AW-DED specimens, there was a difference in the degree of homogenization achieved. The homogenization temperature of 1190 °C was higher than the standard for cast JBK-75 listed in Table II.

Table VII. Hardness Value Comparison

Sample	Hardness (HRB)	Empirical Strength (MPa)[43]
XY Plane AW-DED	102.9 ± 0.39	892
Transverse Plane Wrought	93.5 + 1.6	674
Transverse Plane Cast	98.8 + 1.7	793
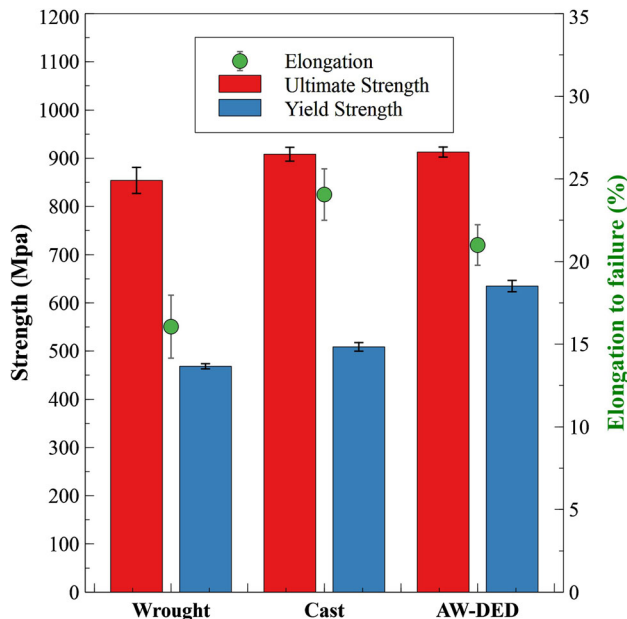
Fig. 14—Mechanical property comparison of three forms of JBK-75 after FHT at room temperature.

Fig. 15—Effects of temperature on the fully heat treated, AW-DED mechanical properties.

Figure 4(a) shows that the cast microstructure was not fully homogenized as remnants of the dendritic structure can still be observed in the optical microscopy images. This is in contrast to the AW-DED specimens in which evidence of a dendritic structure could not be resolved. Although Figure 7 does show striations that could indicate a dendritic structure, elemental differences in these regions could not be resolved. These striations are noted to diffuse in Figure 8.

In metal AM, the metal is deposited and rapidly solidified which is expected to result in finely spaced dendrites. Thus, a higher degree of homogenization is expected as compared with cast material. Since AW-DED also deposits a higher mass of material, the temperature in the part remains elevated during the build. This effectively provides an in situ homogenization.[44,45] Achieving high strength in JBK-75 has been correlated with ensuring a homogenous distribution of Ti.[2,7,10,13]

Table III listed the elemental analysis of the different forms of JBK-75, showing most elements within the specified range for JBK-75.[17] N and O were included in the analysis since the metal AM environment during a build can result in their presence. The primary variations were the Si, Ti and Mn concentrations which have bee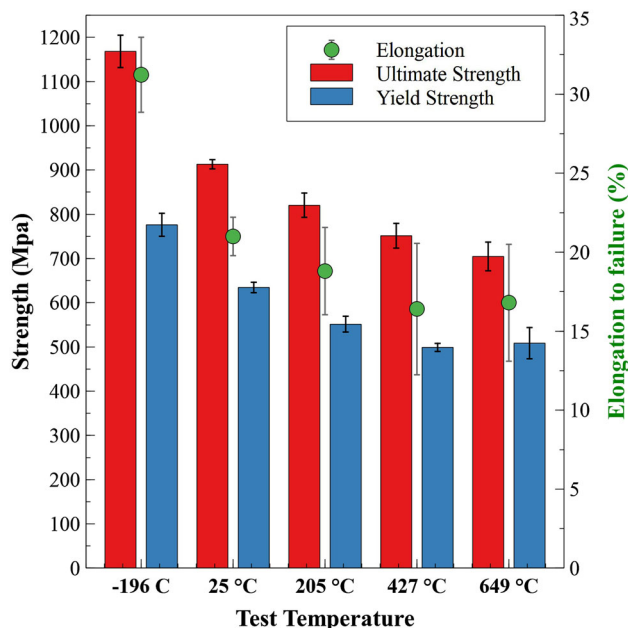n reported to influence the formation of η phase. The presence of C and N present promotes the formation of TiC and TiN, respectively. Although shielding gases are used in AW-DED, oxidation occurs and can form various oxides such as TiO_2 that was observed.

The actual amount of Ti and Al in the AW-DED specimens, as compared to the JBK-75 standard,[17] was slightly reduced.[6,7] This might have been beneficial in reducing the tendency for η formation. Mn was not present in the AW-DED samples and its absence is also noted to reduce the tendency for η formation. The XRD analysis in Figure 13 shows minimal formation of secondary phases in the as-built specimen that correspond to the η and Ti(N,C) phases. Although only one peak is apparent for the minor phases, they correspond to the phases summarized in Table VI.

The XRD analysis correlates with the SEM/EDS images in Figure 7 for the as-built and Figure 8 after the FHT. The EDS maps for the as-built and FHT conditions allow most of the dark particles present to be identified as Ti rich. The Ti rich phases present after the FHT are within the grains and correspond with the XRD indexing of either TiC or TiN in Figure 13. No Ti segregation along grain boundaries was observed in the AW-DED specimens. Some minor gray scale variations are noted within the grains of the AW-DED specimens in the SEM BSE image in Figure 7. This is attributed to possible elemental segregation which fades after the FHT as shown in Figure 8. However, since no detectable elemental variation was detected in the SEM/EDS mapping across the grains and grain boundaries, it is considered to be minor. Comparing the elemental analysis across various grains as well as grain boundaries in Table V again showed no appreciable changes and are consistent with the bulk elemental analysis in Table III.

A very slight indication of the cellular η phase was only observed in the as-built AW-DED specimen, shown in Figures 9 and 10. The small amount was not resolved in the XRD analysis. No similar regions were observed in either the SEM/EDS or XRD after the FHT. Since both the homogenization and solutionizing temperatures were above 800 °C, this would be expected to be effective in driving any η phase present back into the austenitic matrix.[25]

While the majority of the data on metal AM in the literature focuses on the Ni-based superalloys, improved properties of the Fe-based superalloys make their consideration for AM processing of interest. Early literature reported that the properties of JBK-75 were more significantly influenced by the processing route rather than the chemistry.[19–22] Although there were differences in the elongation to failure of the three forms in this study, the strength was similar to the reported UTS of 896 MPa with corresponding elongations greater than 15 pct.[28] As only the AW-DED specimens were fabricated in this study, there is no data pertaining to the thermomechanical processing of the wrought form that would expected to influence the elongation.

A non-reviewed study on laser powder, direct energy deposition (LP-DED)[46] found that homogenization above 1204 °C led to low ductility in the as-deposited samples. Metallurgical evaluation of the as-built sample revealed grain boundaries decorated with η phase that were minimized but not eliminated after the FHT. Ductility was improved if the homogenization temperature was 1093 °C for less than 8 hours. The mechanical properties reported for the LP-DED specimens after a FHT were UTS = 1020 MPa, YS = 730 MPa, and elongation 25–30 pct. No grain sizes were reported for the LP-DED specimens, although the micrographs show a similar grain size to the FHT AW-DED in this study.

A study using laser-powder bed fusion (L-PBF), subjected to a FHT similar to the materials in this study, were tested at a constant strain rate.[47] Although their study was focused on optimizing the parameters, they achieved a UTS = 1180 MPa, YS = 860 MPa and an elongation of 22 pct. Although the strengths were higher in the Neikter, *et al.* study,[47] the as-built specimens displayed Ti and C segregation along the grain boundaries that was successfully dissolved back into the austenitic matrix following the FHT. Thus L-PBF may not be as effective in annealing during the build when compared to the AW-DED process due to L-PBF's lower heat input.

The largest difference in the three forms of JBK-75 was the resulting texture. The XRD analysis indicated random grain orientation in the wrought material as compared to the strong {311} of the cast and {100} of the AW-DED.

For the AW-DED specimens, elevated temperature testing showed little change in the mechanical properties from 427 °C to 650 °C consistent with the upper temperature limit for JBK-75 due to dissociation of the γ' strengthening phase.[3]

V. CONCLUSION

AW-DED is of interest in the fabrication of large components for aerospace and industrial processing applications. The ability to fully homogenize the as-built microstructure of the AW-DED was demonstrated in this study. Fabrication costs can be reduced in the use of AW-DED since it utilizes relatively low-cost equipment and the cored wire can help further reduce cost for custom alloys in small batches. Due to the increased heat and mass input, an initial stress relief to prevent distortion is not required. This study found that the AW-DED deposition of JBK-75 produces mechanical properties similar to cast and wrought material. Since AW-DED is able to produce large parts which may exceed HIP capabilities, the various forms of JBK-75 used in this study were not HIP'd. Thus the use of AW-DED without HIP provides another cost savings.

Key findings in this study include:

– Applicability of AW-DED for reducing costs in metal AM for large components.
– Improved homogenization in AW-DED as compared to casting for similar heat treatment schedules.
– Comparable strength properties noted among three forms of JBK-75, a modified A-286, with differences attributed to solidification texture.
– AW-DED provides a low cost approach toward AM of large components by using standard MIG equipment with fluxless cored wire, that can be customized in small batches.

As the literature shows, the resulting performance of the modified A-286 family of alloys is highly dependent on not only the initial chemistry but also the processing method.

AUTHOR CONTRIBUTIONS

COMPETING INTEREST

REFERENCES

1. G. Parr, A. Hanson, Introduction to Stainless Steels, in: ASM Intl., Metals Park, OH, 1999.
2. D.C. Ludwigson, A.M. Hall: DMIC Report 111, 1959.
3. K.J. Ducki:, in: ed. M. Aliofkhazraei, Superalloys, Intech Open, 2015.
4. N.R. Moody, J.A. Brooks, A.W. Thompson, Development of JBK-75 for service in high pressure hydrogen environments: The role of microstructure, SAND92-8556, 1993.
5. J. Lee, Hydrogen embrittlement, NASA/TM-2016–218602, 2016.
6. T.W. Eichelberger, The response of an iron-base alloy, hardened with titanium to various aging times and temperature, ASM Trans, (1959) 136–149.
7. R. Blower and S. Mayer: *J. Iron Stl. Inst.*, 1963, vol. 201, pp. 933–43.
8. R.F. Decker: *JOM*, 2006, vol. 58(9), pp. 32–36.
9. M.C. Mataya, C.M. Edstrom, R.W. Krenzer, J.H. Doyle, Segregation effects in JBK-75, U.S. Department of Energy, 1979.
10. J.A. Brooks and R.W. Krenzer: *Weld. J.*, 1974, vol. 15, pp. 242s–45s.
11. M.J. Strum, L.T. Summers, and J.W. Morris: *Weld. J.*, 1983, vol. 58, pp. 235s–42s.
12. J.F. Radavich: *Appl. X-Ray Anal.*, 1959, vol. 3, pp. 365–75.
13. J.J. Vagi, R.M. Evans, D.C. Martin, Welding of precipitation-hardening stainless steels, NASA-SP-5087, 1968.
14. J.J. Vagi and D.C. Martin: *Weld. J.*, 1956, vol. 35(3), pp. 137s–44s.
15. B.S. Blum and R.H. Witt: *Weld. J.*, 1963, vol. 42(8), pp. 365s–70s.
16. J.A. Brooks: *Weld. J.*, 1974, vol. 8, pp. 517s–23s.
17. J.A. Brooks, R.W. Krenzer, US Patent #3895939 for JBK-75, July 22, 1975.
18. A.W. Thompson and J.A. Brooks: *Met. Trans. A*, 1975, vol. 6A, pp. 1431–42.
19. T.J. Headley, M.M. Karnowsky, and W.R. Sorenson:*Met. Trans*, 1982, vol. 13A, pp. 345–54.
20. M.C. Mataya, M.J. Carr, and G. Krauss: *Met. Trans.*, 1984, vol. 15A, pp. 347–68.
21. R. Frisk, M.A.I. Andersson, and B. Rogbeg: *Metals (Basel)*, 2019, vol. 9, p. 711. https://doi.org/10.3390/met9060711.
22. K. Metcalf: *Iron Age*, 1958, vol. 182, pp. 73–74.
23. S. Chen, M. Zhao, and L. Rong: *Mater. Sci. Eng. A*, 2013, vol. 571, pp. 33–7.
24. L. Xiuyan, Z. Jian, R. Lijian, and L. Yiyi: *Mater. Sci. Eng.*, 2008, vol. 488, pp. 547–53.
25. M. Seifollahi, S.H. Razavi, Sh. Kheirandish, and S.M. Abbasi: *Phys. Metals Metall.*, 2020, vol. 121(3), pp. 322–29.
26. M.J. Zhao, Z.F. Guo, H. Liang, and L.J. Rong: *Mater. Sci. Eng.*, 2010, vol. 527, pp. 5844–851.
27. M.S. Qurashi, Y. Zhao, C. Dong, X. Zhang, L. Wang, Y. Li, and P. Wan: *Steel Res. Int.*, 2022, vol. 93, pp. 1–3.
28. SAE/AMS 5732, Steel, Corrosion and Heat-Resistant, Sheet, Strip, and Plate 15 Cr -25.5Ni - 1.2 Mo − 2.1 Ti - 0.006B − 0.3V, Consumable Electrode Melted, 1800 °F (982 °C) Solution heat treated.
29. J.A. Schneider, Mechanical property improvement study for the JBK-75 alloy in the cast form, MS Thesis, University of California, Davis, 1993.
30. Aerospace Structural Metals Handbook, Code 1601, Printed March 1987.
31. S.W. Williams, F. Martina, A.C. Addison, J. Ding, G. Pardal, and P. Colegrove: *Mater. Sci. Tech.*, 2016, vol. 32(7), pp. 641–47.
32. P. Gradl, D. Tinker, A. Park, O. Mireles, M. Garcia, R. Wilkerson, and C. McKinney: *J. Matl. Eng. Perf.*, 2021, vol. 31, pp. 6013–44. https://doi.org/10.1007/s11665-022-06850-0.
33. P.R. Gradl, et al., Chapter 2: metal additive manufacturing for propulsion applications, in: P. Gradl, C. Protz, O.R. Mireles, C. Garcia (eds), Metal Additive Manufacturing Processes and Selection, Progress in Astronautics and Aeronautics, 2022, pp. 49–186.
34. C. Kantzos, Chapter 6: feedstock for metal additive manufacturing in: P. Gradl, C. Protz, O.R. Mireles, C. Garcia (eds), Metal Additive Manufacturing Processes and Selection, Progress in Astronautics and Aeronautics, 2022, pp. 405–438.
35. Polymet, https://www.polymet.us/. Accessed January 2020.
36. ASTM E3047-16, Standard Test Method for Analysis of Nickel Alloys by Spark Atomic Emission Spectrometry, ASTM International, West Conshohocken, PA, 2016.
37. ASTM E1019-18, Standard Test Methods for Determination of Carbon, Sulfur, Nitrogen, and Oxygen in Steel, Iron, Nickel, and Cobalt Alloys by Various Combustion and Inert Gas Fusion Techniques, ASTM International, West Conshohocken, PA, 2018.
38. ASTM E8/E8M-21, Standard Test Methods for Tension Testing of Metallic Materials, ASTM International, West Conshohocken, PA, 2021.
39. ASTM E18-22, Standard Test Methods for Rockwell Hardness of Metallic Materials, ASTM International, West Conshohocken, PA, 2022.
40. ASTM E112-96, Standard Test Methods for Determining Average Grain Size, ASTM International, West Conshohocken, PA, 1996.
41. M. Seifollahi, S.H. Razavi, Sh. Kheirandish, and S.M. Abassi: *JMEPEG*, 2013, vol. 22, pp. 3063–69.
42. J.A. Schneider, et al., Chapter 4: Metal AM materials microstructure and properties in: P. Gradl, C. Protz, O.R. Mireles, C. Garcia (eds), Metal Additive Manufacturing Processes and Selection, Progress in Astronautics and Aeronautics, 2022, pp. 327–306.
43. https://www.steelexpress.co.uk/steel-hardness-conversion.html. Accessed April 2023.
44. J. Stone, Predicting Resultant Microstructure of an Additive Manufactured Build with a Global Transient Thermal Model, MS Thesis, College of Engineering, 2020.
45. J.A. Schneider, P. Gradl, Directed Energy Deposition moves outside the box, AM&P, 2022.
46. A. Birken, D. Noel, Metallurgical and thermal processing investigation of additively manufactured superalloys JBK-75 and NASA HR-1, Senior project, California Polytechnic State University, San Luis Obispo, 2021.
47. M. Neikter, P. Bhaskar, S. Singh, K. Kadoi, C. Lyphout, F. Svahn, and R. Pederson: *Mater. Sci. Eng.*, 2023, vol. 874, 144911.